Evidence for liquid-liquid phase separation during the early stages of Mg-struvite formation

Stephanos Karafiludis ✉ ; Ernesto Scoppola ; Stephan E. Wolf ; Zdravko Kochovski ;
David Matzdorff; Alexander E. S. Van Driessche ; Jörn Hövelmann; Franziska Emmerling ;
Tomasz M. Stawski ✉

Check for updates

CrossMark

View
Online

Export
Citation

Evidence for liquid-liquid phase separation during the early stages of Mg-struvite formation

View Online   Export Citation   CrossMark
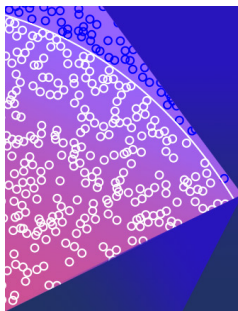
Stephanos Karafiludis,[1,2,a] (iD) Ernesto Scoppola,[3] (iD) Stephan E. Wolf,[4] (iD) Zdravko Kochovski,[5] (iD)
David Matzdorff,[5] Alexander E. S. Van Driessche,[6] (iD) Jörn Hövelmann,[7] Franziska Emmerling,[1,2] (iD)
and Tomasz M. Stawski[1,a] (iD)

AFFILIATIONS

[1] Federal Institute for Materials Research and Testing (BAM), Richard-Willstatter-Straße 11, 12489 Berlin, Germany
[2] Department of Chemistry, Humboldt-Universität zu Berlin, Brook-Taylor-Straße 2, 12489 Berlin, Germany
[3] Biomaterials, Hierarchical Structure of Biological and Bio-inspired Materials, Max Planck Institute of Colloids and Interfaces, Potsdam 14476, Germany
[4] Friedrich-Alexander University Erlangen-Nürnberg (FAU), Department of Materials Science and Engineering, Institute for Glass and Ceramics, Martensstr. 5, 91058 Erlangen, Germany
[5] Helmholtz-Zentrum Berlin for Materials and Energy, Hahn-Meitner Platz 1, 14109 Berlin, Germany
[6] Instituto Andaluz de Ciencias de la Tierra (IACT), CSIC – Universidad de Granada, Av. De las Palmeras 4, 18100 Armilla, Spain
[7] REMONDIS Production GmbH, Brunnenstraße 138, 44536 Lünen, Germany

[a] Authors to whom correspondence should be addressed: tomasz.stawski@bam.de and stephanos.karafiludis@bam.de

ABSTRACT

The precipitation of struvite, a magnesium ammonium phosphate hexahydrate ($MgNH_4PO_4 \cdot 6H_2O$) mineral, from wastewater is a promising method for recovering phosphorous. While this process is commonly used in engineered environments, our understanding of the underlying mechanisms responsible for the formation of struvite crystals remains limited. Specifically, indirect evidence suggests the involvement of an amorphous precursor and the occurrence of multi-step processes in struvite formation, which would indicate non-classical paths of nucleation and crystallization. In this study, we use synchrotron-based *in situ* x-ray scattering complemented by cryogenic transmission electron microscopy to obtain new insights from the earliest stages of struvite formation. The holistic scattering data captured the structure of an entire assembly in a time-resolved manner. The structural features comprise the aqueous medium, the growing struvite crystals, and any potential heterogeneities or complex entities. By analysing the scattering data, we found that the onset of crystallization causes a perturbation in the structure of the surrounding aqueous medium. This perturbation is characterized by the occurrence and evolution of Ornstein-Zernike fluctuations on a scale of about 1 nm, suggesting a non-classical nature of the system. We interpret this phenomenon as a liquid-liquid phase separation, which gives rise to the formation of the amorphous precursor phase preceding actual crystal growth of struvite. Our microscopy results confirm that the formation of Mg-struvite includes a short-lived amorphous phase, lasting >10 s.

INTRODUCTION

The precipitation of struvite (magnesium ammonium phosphate hexahydrate, $MgNH_4PO_4 \cdot 6H_2O$) from wastewater is one of the most promising phosphorous recovery methods. This approach is already implemented to a limited extent,[1–4] with no fewer than 40 industrial-scale treatment plants in operation worldwide, capable of mineralising up to 25% of the dissolved P from their agricultural waste stream.[3–10] The recovered material is used as a phosphate replacement for natural ore deposits, i.e. phosphorites, or is consumed directly as a slow-release fertiliser. In addition, struvite formation can be locally problematic as it forms dense, persistent scale in pipes or filters, fouling and clogging components in water treatment plants. Therefore, struvite precipitation needs to be

optimised to increase efficiency or to reduce the unintended occurrence of rapidly forming scale in engineered environments. One of the major challenges in achieving this goal is to understand the formation pathways of struvite from the early stages. For instance, the ability to detail specific stages of the crystallisation or the occurrence of transient (amorphous) precursors would allow for the development of targeted growth additives (e.g. water-soluble polymers) that give control over crystal shape, size or that stabilise intermediate stages.[11]
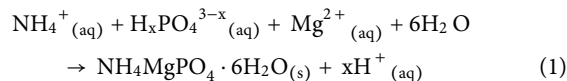
Over the last few decades, the advent of new and/or improved observation tools revealed the remarkable complexity of the formation process of minerals from aqueous solutions. The dominance of the original "textbook" picture of these phenomena, derived from the adaptation of classical nucleation and growth theories (CNT), has faded, and classical one step formation pathways are complemented by more complex multistep, so-called "non-classical" nucleation and crystallisation pathways. These pathways comprise a variety of precursor and intermediate species, including solute colloidal entities, e.g., prenucleation clusters (PNCs), liquid(-like) phases, amorphous and nanocrystalline solids, or mesocrystals leading to the formation of the final crystals through multistep and self-assembly mechanisms.[12] Most of our knowledge and intuition about non-classical crystallisation[12] come from the studies on mineral systems of metal carbonates,[13–17] phosphates,[18–23] sulfates[24–27] or iron oxides.[28–30] In these systems, the precursor species persist long enough (typically for at least several seconds to hours) to be observed and, thus, further investigated.

On the other hand, for some minerals, the ephemeral nature and low concentrations of potential precursor/intermediate species may hinder a possibility to be captured, leading to the potentially incorrect conclusion that such systems behave classically. This is particularly true for Mg-struvite,[31] which has yet to provide clear evidence of involving an amorphous precursor, despite observations of amorphous-like species under specific conditions.[11,20] Here, we demonstrate that the Mg-struvite formation involves a short-lived (<10 s) amorphous phase, pointing towards a non-classical nature of the system. Furthermore, we show that the onset of crystallisation manifests itself as a perturbation in the structure of the aqueous medium in which the process takes place. This perturbation potentially indicates a liquid–liquid phase separation (LLPS) as the origin of the amorphous precursor which precedes the actual crystal growth phase.[32]

MATERIALS AND METHODS

Materials and synthesis

$(NH_4)_2HPO_4$ (DAP) (ChemSolute, 99%) and $MgCl_2 \cdot 6H_2O$ (ChemSolute, 99%) were used to synthesise struvite. The experiments were carried out in equimolar concentrations of 0.1 M for $MgCl_2$ and DAP resulting in a metal-to-phosphate ratio of 1. These aqueous solutions were prepared by dissolving the calculated amount of salt in deionised water (>18 MΩ cm). Generally, struvite forms in a simple "one pot" approach, where typically equal volumes of DAP and Mg-bearing solutions are mixed in a beaker using a magnetic stirrer (500 rpm) at (20 °C, according to the mass-balance equation [Eq. (1)]. We describe the specific reaction procedures below.

$$NH_4^+{}_{(aq)} + H_xPO_4^{3-x}{}_{(aq)} + Mg^{2+}{}_{(aq)} + 6H_2O$$
$$\rightarrow NH_4MgPO_4 \cdot 6H_2O_{(s)} + xH^+{}_{(aq)} \quad (1)$$

We also explored the reaction from Eq. (1) for our conditions in terms of speciation and equilibrium concentrations by performing thermodynamic modelling with PHREEQC v. 3.[33] The input and output files from the software are included in the supplementary material.

pH measurements

The reaction progress was followed *in situ* at 20 °C by measuring pH as protons were released during precipitation [Eq. (1)]. The pH was continuously measured with a pH electrode connected to a data logger board DrDAQ with a time resolution of 1 s (Pico Technology, Cambridgeshire, UK). The measured pH ranged from the initial 0.1 M DAP solution at around 8.0 to the end of precipitation at 5.8. Before the experiments, the pH electrode was calibrated against buffer solutions.

Thermodynamic calculations

The pH measurements were evaluated and verified by calculations with the aqueous geochemical simulation program PHREEQC v. 3 using the Wateq4f database (wateq4f.dat)[33,34] and displayed in the supplementary material (supplementary material: Fig. S1). Any missing database entries for the relevant Mg-containing phases were completed with literature K_{sp} values.[35,36] The thermodynamic modelling of the precipitation reaction [Eq. (1)], using our starting conditions as input, with PHREEQC (supplementary material: Input/Output files) indicates that the intrinsic yield of struvite precipitation was ~46% at the equilibrium. This means that the final aqueous solution was equilibrated with crystals at ~0.33% of the volume fraction (M_w = 245.41 g/mol; d = 1.71 g/cm^3), which was sufficient to measure scattering patterns with an acceptable signal-to-noise ratio on our instrument (see below).

Flow-through setup for scattering

All the scattering experiments were performed using a polyether ether ketone flow-through cell coupled with a pump setup. 50 ml of a 0.1 M DAP solution was stirred (500 rpm) in a 200 ml glass reactor. The content of the reactor was continuously circulated through a borosilicate glass capillary cell (ID = 1.498 mm) using a peristaltic pump (Longer BT100-2J) at 300 ml/min. A schematics of the experimental setup can be found in the SI (supplementary material: Fig. S3). The dead volume of tubing was ~2 ml. 50 ml of a $MgCl_2$ solution was injected into the reactor containing DAP at 300 ml/min using a second peristaltic pump with a remote control. The injection of the solution took 10 s to complete. The pH measurements (DrDAQ data logger board, PicoLog 6 software, Pico Technology, Cambridgeshire, UK) were performed every 1 s for the entire duration of the experiment. The scattering data were collected at 10 s/frame. The time scales of all the measurements/experiments were aligned according to the following convention: the measurement finishing at 0 s (thus starting at negative 10 s) represents a structure of an unmixed solution (i.e. only DAP), the measurement at 10 s represents the averaged structure of the solution until

the end of the injection, the measurement at 20 s corresponds to stoichiometrically mixed solutions.

Synchrotron-based scattering

X-ray scattering measurements were performed on the mySpot beamline[37] of BESSY-II (Helmholtz-Zentrum Berlin, HZB, Germany), using a monochromatic x-ray beam at 15.0 keV aligned with a capillary of the flow-through setup at 20 °C. Scattered intensities, small- and wide-angle x-ray scattering (SAXS/WAXS) were collected with a large-area Dectris Eiger 9M detector as a single continuous signal. The sample-to-detector distance of ~330 mm allowed for a usable q-range of ~$0.1 < q < 39$ nm^{-1}. Transmission through the sample was calculated using an x-ray fluorescence signal collected from a lead beamstop using a RAYSPEC Sirius SD-E65133-BE-INC detector equipped with an 8 μm beryllium window, where the incoming beam intensity was monitored and normalised using an ion chamber. The scattering q-range was calibrated against silicon (NIST SRM640) and the corresponding measured intensity was calibrated to absolute units against water (at 20 °C) and a glassy carbon standard (NIST SRM3600, 1 mm). The resulting data were processed with custom Python scripts utilizing a pyfai library.[38] The processing steps included integration to 1D scattering curves and subtraction of an instrumental background (i.e. an "empty beamline" or "air" background). The resulting scattering data were corrected for transmission and scaled to absolute intensity units. The as-obtained raw scattering curves were further corrected for an empty capillary background.

We used a circular beam, ~100 μm in diameter, which was collimated by a series of pinholes. The beam profile was also measured to account for the instrumental effects on the diffraction parameters, and to take in account the beam divergence, the energy resolution and the detector pixel size. This was performed by scanning the beam vertically and horizontally across two perpendicular 0.1 mm tungsten wires. The diffraction peaks were separated from the scattering data by applying an Asymmetric Least Square Smoothing baseline correction method,[39,40] and selected characteristic peaks were fitted with pseudo-Voigt functions convolved with the q-dependent Gaussian instrumental smearing function to extract information about their positions, broadening values and areas as a function of time.

Cryogenic transmission electron microscopy

50 ml of 0.1 M DAP solution was stirred (500 rpm) in a 200 ml glass reactor. 50 ml of a magnesium chloride solution was injected (~10 s) into the reactor containing DAP at 300 ml/min using a peristaltic pump (Longer BT100-2J). Aliquots of struvite solutions were taken directly from the reactor, 5 and 60 s after mixing.

Cryo-TEM imaging was performed using a JEOL JEM-2100 transmission electron microscope (JEOL GmbH, Eching, Germany). Specimens were prepared by casting a 4 μl droplet of the aliquot solutions onto lacey carbon-coated copper TEM grids (200 mesh, Electron Microscopy Sciences, Hatfield, PA), and plunge-frozen into liquid ethane using an FEI vitrobot Mark IV set at 4 °C and 95% humidity. Vitrified grids were either transferred directly to the microscope's cryo-transfer holder (Gatan 914, Gatan, Munich,

Germany) or stored in liquid nitrogen. All grids were glow-discharged before use. Imaging was carried out at temperatures around −180 °C. The TEM was operated at an acceleration voltage of 200 kV, and an objective lens defocus of about 1.5–2 μm was used to increase the contrast. Micrographs were recorded with a bottom-mounted 4·4 K CMOS camera (TemCam-F416, TVIPS, Gauting, Germany). Each micrograph's electron dose was kept below 20 e/Å^2 to minimise any potential beam damage to the samples. All images were processed using ImageJ2.[41]

RESULTS AND DISCUSSION

An overview of the crystallisation progress

According to Eq. (1), the precipitation of struvite results in the release of protons, and therefore the evolution of pH can serve as a chemical proxy for the reaction kinetics [Fig. 1(a), supplementary material: Fig. S1]. Within the time resolution constraints of our experiment, it is evident that nucleation and crystallisation of struvite was occurring within ~60 s after mixing i.e. until a plateau at pH ~5.8 was reached, down from the initial ~7.9. Figure 1(b) shows the evolution of the most intense diffraction peak of struvite [at $q = 14.74$ nm^{-1}; (111), (11-1)[42]], in accordance with the pH profile. The inset in Fig. 1(b) provides time-resolved diffraction patterns confirming that struvite is the only crystalline phase forming in solution at all times. The diffraction data indicate that struvite started to crystallise after 10 s, which is corroborated by the pH trend. Starting a t = 0 s, pH starts to drop from an initial ~7.9 due to the addition of a neutral solution (MgCl$_2$, pH ~7.0) and the release of protons that originated from the precipitation. The crystal growth process continued for ~60 s and beyond, following the evolution of the pH profile. The experimentally determined equilibrium (i.e. final) pH is in close agreement (ΔpH = ±0.05) with the predicted value obtained from PHREEQC calculations (supplementary material: Fig. S1).

Based on the diffraction and pH data, one can expect that at <10 s and further at 60 s, we should observe different phases and morphologies. Indeed, to evaluate what happened during the first minute after mixing, we sampled and cryo-quenched the solution after 5 and 60 s of mixing. Figure 2(a) shows the morphology of particles present after 5 s. At low magnification [Fig. 2(a), left], one can observe aggregates of particles (see arrows) predominantly embedded into thicker vitrified ice (purple false colour). A higher magnification imaging [Fig. 2(a), middle] revealed that these aggregates are composed of near-spherical particles with diameters of ~40 to 50 nm. Selective area electron diffraction (SAED) from the aggregates [Fig. 2(a), right] indicated that the observed particles were amorphous. The inset in Fig. 2(a), highlights that these amorphous particles coalesce and are of low-electron density, which could be an indicator of an originally liquid-like character[43,44] before cryo-quenching. After 60 s micrometer-sized single crystals of struvite readily developed in the solution [Fig. 2(b), left and middle], as was evident from the observed characteristic faceting, and the SAED exhibited only single diffraction spots assigned to struvite[42] [Fig. 2(b), right]. The morphology of the amorphous particles and their aggregates in Fig. 2(a) is emulsion-like. Such structures have been observed for other systems with a prevalent amorphous phase and have been interpreted as a consequence of a liquid-liquid phase
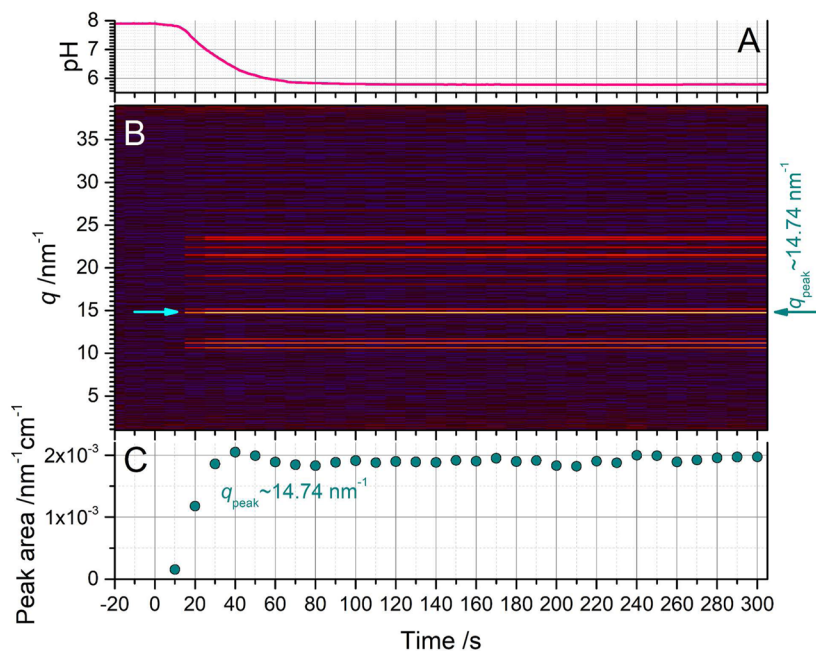
FIG. 1. (a) The pH curve corresponds to the *in situ* scattering experiment. At t = 0 s, the two reactants begin to mix to precipitate struvite, and at t = 10 s, a stoichiometrically mixed solution is obtained; (b) The complete time-resolved diffraction pattern of struvite up to 300 s; a characteristic peak at $q = 14.74$ nm^{-1} is marked with the arrows; (c) Evolution of the integrated area of a diffraction peak of struvite at $q = 14.74$ nm^{-1}. (a)–(c) share the time axis.

separation process preceding crystallisation.[13,17,45–48] Considering data and trends from Figs. 1 and 2, the amorphous phase is struvite in short-lived and persists for ~10 s, for our experimental conditions. In comparison with other non-classical mineral systems, it is a relatively short period and some amorphous phases in solutions can persist for hours.[20,49–52] We note however that since crystallisation depends significantly on a variety of reaction physicochemical conditions, it is hard to compare the absolute time scales among different chemical systems.

General structural features and the scattering model

We used the broad q-range (0.1–45 nm^{-1}) of the single-detector SAXS/WAXS to track the changes taking place upon struvite formation. Our *in situ* scattering approach provided a holistic view of the structural evolution of the solid struvite phase (Fig. 1) and the surrounding aqueous solution. The experimental configuration allowed for a time resolution of 10 s/frame. Despite the relatively slow injection, mixing and pumping times, the 10 s resolution was sufficient to capture several snapshots of the early-stage struvite evolution before reaching equilibration at ~60 s (Fig. 1). Below, we describe the observable features in the patterns, based on which we formulate a model to quantify them. In the next steps, we interpret the evolution of struvite based on the identified scattering features and the as-derived fitting parameter values.

In all the curves shown in Fig. 3(a), two broad maxima are observed at ~20 and ~29 nm^{-1}, characteristic for water (or diluted aqueous solutions in our case).[53–59] The main peak at ~20 nm^{-1} originates from the O–O average spacing of ~3.1 Å. The second peak

at ~29 nm^{-1}, often classified as a shoulder of the first peak, represents the tetrahedral structure in the water network. Moreover, from the perspective of the aqueous medium, there is a plateau in intensity $[I(q) \propto q^0]$ for the range of $0.5 < q < \sim 2$ nm^{-1}, whose position normally corresponds to the isotropic compressibility of water.[54,60] It is also proportional to the square of the scattering length density contrast of the aqueous medium. In the intermediate range $4 < q < 10$ nm^{-1}, we observe a local minimum, which can be attributed to Ornstein-Zernike (OZ) density fluctuations.[54,59,61,62] The intensity decrease for $q < 0.2$ nm^{-1}, seen only at 0 s, is a common artefact of the background (an empty capillary) subtraction in water.[60,62]

The scattering curve at 0 s in Fig. 3(a) depicts the initial structure of the aqueous 0.1 M DAP solution. The scattering patterns changed after mixing at 10 s, when a 0.05 M struvite "solution" was formed, and continued to evolve until 300 s. Accordingly, at 10 s and thereafter, we observe a steep increase for $q < 0.5$ nm^{-1}, following an approximate $I(q) \propto q^{-4}$ relationship and corresponds to the formation of large scattering Porod interfaces.[63,64] Starting from 10 s, also multiple narrow diffraction peaks start to appear at $q > 10$ nm^{-1}, which correspond to characteristic Bragg reflections of struvite (see also Fig. 1).

Based on the above scattering features, the curves are interpreted by fitting the model summarised in Eq. (2).

$$I\left(q, I_0, I_1, I_2, D, \xi oz, d, \xi_{peak}, m, bkg\right) \simeq$$
$$\simeq I_0 q^{-D} + \frac{I_1}{1 + q^2 \xi_{oz}^2} + \frac{I_2}{1 + \left(\left|q - \frac{2\pi}{d}\right| \xi_{peak}\right)^m} + bkg \quad (2)$$
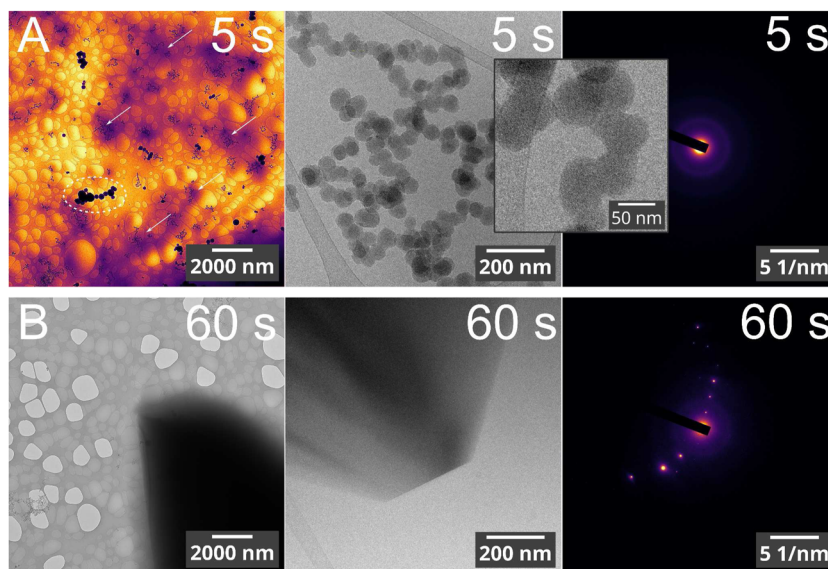
FIG. 2. Cryo-TEM bright-field imaging and diffraction from the reactant solution sampled after (a) 5 s after mixing; (b) 60 s after mixing; (left column) low-magnification; (middle column) high-magnification; (right column) SAED pattern. Selected images in false colour, "inferno: scale. Selected aggregates of amorphous particles are indicated with white arrows. The inset in (a) highlights the presence of coalesced amorphous particles. The white dashed ellipse in (a) marks an example of ice crystals as contaminants, which has a form of larger black spheres. The lacey film of the grid is also visible. To prevent any potential misinterpretations potentially introduced by using a colour scale, we show the grey-scale image of (a) in the supplementary material (supplementary material: Fig. S2).

In Eq. (2), the sum consists of three structural components and a background constant, *bkg*. Below, we explain in detail all the used variables. This model does not account for the diffraction peaks of crystalline phases.

The first contribution, which is proportional to a constant I_0, describes scattering from Porod interfaces manifesting themselves at 10 s and thereafter. The scattering originates from large objects, i.e. μm-sized particles $\gg d_{max}$, relative to the available q-range, where $q_{min} = 0.1$ nm^{-1} and $d_{max} = 2\pi/q_{min}$. Here, the exponent D is associated with a fractal dimension, and takes values $3 < D \leq 4$, where D = 4 represents a smooth interface, while D < 4 indicates rough, surface-fractal-like objects.[63] The scaling constant I_0 is proportional to a specific surface area, i.e., the particle's surface and volume ratio.

The second term, proportional to scaling constant I_1, is the Ornstein-Zernike (OZ) form factor of liquid density fluctuations, typically observed in the presence of critical points.[54,62] The parameter ξ_{OZ} is the correlation length of such fluctuations.

The third and final term, proportional to a scaling constant I_2, represents a broad peak[62] with a centroid at $2\pi/d$, where d is a characteristic Bragg spacing; m is an exponent that expresses the shape of a peak function (m = 2 for a Lorentzian); and ξ_{peak} is a spatial extent of a scattering domain associated with d.

Figure 3(b) provides an example of fitting with the model from Eq. (2), including the contributions of each component to a scattering curve. We see that the Porod term (proportional to I_0) in Eq. (2) mainly contributes at low q values ($q < 0.5$ nm^{-1}), and reflects the scattering from large particles such as struvite crystals. On the other hand, the OZ term (proportional to I_1) contributes to scattering at supramolecular length scales at $0.5 < q < \sim10$ nm^{-1}, and measures the extent of fluctuations in the aqueous medium's structure. The

$I(q) \propto q^0$ plateau ($0.5 < q < 2$ nm^{-1}) and the local intensity minimum ($4 < q < 10$ nm^{-1}) are modelled by this term. Nominally, we may consider two peaks to model the structure of an aqueous medium for $q > 10$ nm^{-1}, due to the presence of two maxima with centroids at q of ~20 and ~29 nm^{-1}. However, they cannot be accurately fitted with only two functions, each in the form of our broad peak expression [i.e. I_2-dependent in Eq. (2)], or by other peak functions such as the pseudo-Voigt. Moreover, the peak feature in water at ~29 nm^{-1} is known to evolve into a mere shoulder with increasing temperatures.[57] As mentioned before, the considered part of the scattering pattern manifests the molecular-level structure of water and can be merely approximated with simple functions as the one in Eq. (2). Additional terms or asymmetric peak functions should be used, which would account for polydispersity in network O–O distances and the tetrahedral structure of water.[53–59] To simplify this issue, we use a single broad peak expression in Eq. (2) and only for q up to ~21.3 nm^{-1}. This way, we correctly represent the rising shoulder of the peak, to account for a crossover with the OZ contribution preceding the peak. Thus, the extracted values of d and I_2 are interpretable, while ξ_{peak} and m become mere parameterizations of the peak's shape (see the extrapolated fitting curve in Fig. 3(b). The fit parameters for the entire series are summarised in Fig. 4. We excluded the trend in d as it was practically constant at $d = 0.311 \pm 1.0 \times 10^{-4}$ nm for all the curves.

Formation of struvite in scattering

Following the evolution of the system in Fig. 3(a), one can observe that as the solution progresses from 0 s (pre-mixing) to 10 s (post-mixing) and beyond, the evolution of the scattering curves
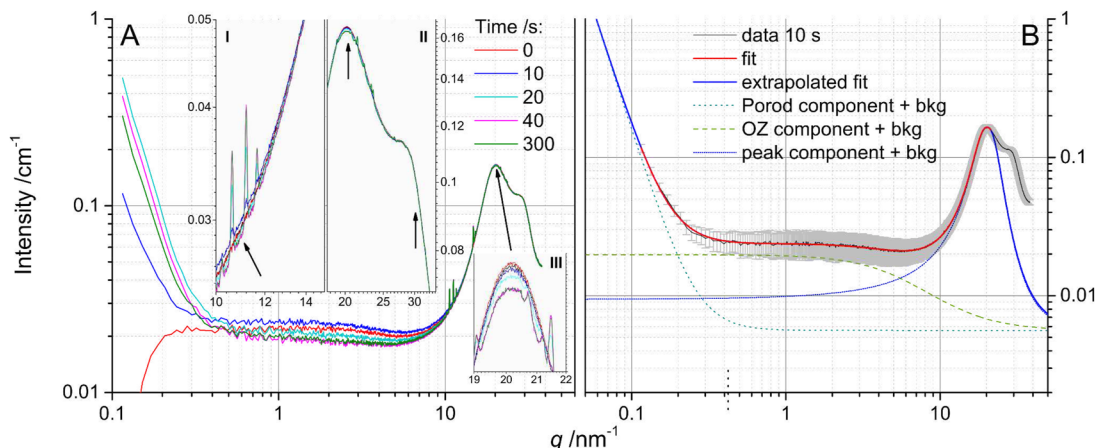
FIG. 3. (a) Selected *in situ* scattering curves at different moments of time; the diffraction peaks correspond to struvite and are the same as those in Fig. 1; inset I highlights, changes for $10 < q < \sim14$ nm^{-1} where the baseline intensity decreases as the diffraction peaks gradually develop (see the arrow); insets II and III highlight the changes in the scattering curve where the maximum of the broad peak at $q \sim20$ nm^{-1} decreases upon the evolution of the crystals, while the scattering around the second maximum at $q \sim29$ nm^{-1} remains unchanged throughout the entire processes up to 300 s; measurement uncertainties are not shown for clarity; B) a dataset at 10 s fitted with the model from Eq. (2) up to $q < 21.3$ nm^{-1}; individual contributions of the model components are plotted; the fitted curve was extrapolated beyond the fitting q-range; all curves according to the labels; fit parameter values, $I_0 = 4.966\,98 \times 10^{-5} \pm 1.801\,52 \times 10^{-6}$ cm^{-1}, $D = 3.4925 \pm 0.017\,79$, $I_1 = 0.014\,15 \pm 1.565\,37 \times 10^{-4}$ cm^{-1}, $\xi_{OZ} = 0.165\,36 \pm 0.001\,93$ nm, $I_2 = 0.158\,15 \pm 1.968\,71 \times 10^{-4}$ cm^{-1}, $d = 0.310\,99 \pm 1.021\,47 \times 10^{-4}$ nm, $\xi_{peak} = 0.242\,38 \pm 3.778\,02 \times 10^{-4}$ nm, m = 2.330 66 $\pm$ 0.0063; $bkg = 0.005\,64 \pm 2.067\,36 \times 10^{-4}$ cm^{-1}.

clearly reflects the formation of struvite. In terms of the magnitude of changes in the intensity, the most obvious ones are associated with the evolution of the Porod interfaces for $q < 0.5$ nm^{-1} [the 1st term in Eq. (2)]. Therefore, we first consider the evolution of the fit parameters I_0 and D shown in Fig. 4 [from fitting with Eq. (2), Fig. 3(b)]. We also prompt that the 10 s frame marks the onset of the appearance of the diffraction peaks of struvite [Figs. 1(b) and 3(a)]. The diffraction peaks fully develop throughout 20–40 s frames, and simultaneously the low-q Porod interface intensity [Fig. 3(a)] and the associated parameter I_0 increase (Fig. 4), which is consistent with increasing specific surfaces due to the nucleation of new crystals. Therefore, we associate the evolution of Porod interfaces predominantly with the growth of crystalline solids. The value of D remains constant at ~3.5 through the reaction, indicating atomically rough surfaces, a fact we previously observed for other crystal systems in solution[63] (with a value of $D = 4$ for ideal smooth Porod interfaces). The constancy of the trend is highly significant because it suggests that we are only dealing with ongoing crystal growth without the development of other morphological features, such as mass-fractal aggregates of nano-sized particles.[63]

We highlight that the Porod intensity reduction observed at 300 s in Fig. 3(a), and the matching reduction in I_0 in Fig. 4, may appear counterintuitive for a system which "grows." However, this effect can be explained by considering crystals that have grown beyond the detectable size range for the available q-range. To account for this, we introduce a simplified sphere equation,[63] considering two populations of "particles" (Eq. (3)) with radii R_0 and R_1, and the same scattering contrast $\Delta\rho$:

$$I(q, n, \phi, \Delta\rho, R_0, R_1) = (1-n)\phi(\Delta\rho)^2 \cdot 4/3\pi R_0{}^3 \cdot \frac{1}{1 + 2/9(qR_0)^4}$$
$$+ n\phi(\Delta\rho)^2 \cdot 4/3\pi R_1{}^3 \frac{1}{1 + 2/9(qR_1)^4} + bkg \tag{3}$$

The total volume fraction of solids is denoted by ϕ, and each population's contribution is expressed by a weighting factor $0 \leq n \leq 1$, maintaining the total volume fraction constant. Now let us consider a scenario with only one dominant size of particles, when $n = 0$. By using Eq. (3) we can simulate the contributions of the larger crystals and estimate their Porod intensity reduction. In Fig. 5(a) we evaluate the contributions of such a single population. Within our q-range ($q_{min} > 0.1$ nm^{-1}), only spherical particles with $R = \sim10$ nm would exhibit clear form factors, while larger sizes would appear as Porod interfaces at different intensities. As the radii of the particles increase, their scattering curves migrate towards lower q-values. Consequently, the intensity within our q-range window actually decreases, although it increases at even lower q-values outside our range. Considering that the intensity in Eq. (3) depends on the radius, electron density contrast, and volume fraction, it is practically impossible to discriminate among these contributions in our experiments just by considering a single curve without a context of the entire time series. Since we do not know ϕ or $\Delta\rho$ a priori, which may also evolve during the precipitation processes, we cannot determine the particle radii directly. However, since our data are time-resolved, and it is logical to assume that crystals grow from small to large sizes, the decrease of Porod intensity at 300 s [Fig. 1(a)]
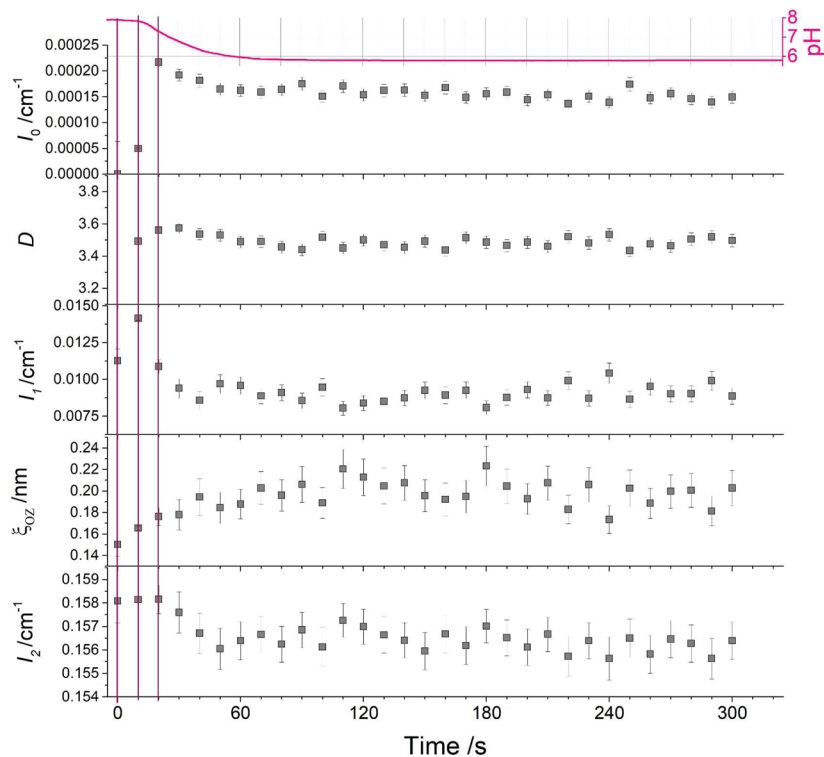
FIG. 4. Evolution of I_0, D, I_1, ξ_{OZ}, and I_2 over the 300 s after the injection of the metal salt solution. Already after the 60 s, most parameters reach plateau values, indicating no further significant changes in the precipitation processes. We do not include the trend in d [Eq. (2)], which was practically constant at $d = 0.311 \pm 1.0 \times 10^{-4}$ nm for all the curves.

is explained by the growth of crystals towards larger sizes. Furthermore, by Definition I_0 is proportional to a specific surface area. Thus, for a constant electron density contrast, its evolution in Fig. 4 should follow a $I_0 \sim 1/radius$ dependence for growing particles, which is indeed the case. This would be rationalised by the scenario in which no new crystals are nucleating, and instead the already existing ones grow (see Fig. 5) and Fig. 5(a).

Building on this explanation, we now investigate why no amorphous particles are directly observed in the scattering patterns, despite their radii of ~20–25 nm [cryo-TEM, Fig. 2(a)] being well within our q-range. In this regard, we did not observe any obvious form-factor-like features for $q > ~1$ nm^{-1} in Fig. 3(a) that could be attributed to such particles. The bottom line assumption is the coexistence of amorphous precursor nanoparticles next to much larger scattering features such as struvite crystals, which contrastingly manifest themselves as Porod interfaces. This scenario is modelled by Eq. (3), where $n \neq 0$. In Fig. 5(b), we evaluated how different amounts of 500 and 25 nm particles would contribute to a scattering pattern by varying n in Eq. (3), from 1% to 50%. Within our available q-range, we could only observe Porod interfaces at different intensities, denying any possibility to discern contributions from smaller amorphous particles among significantly larger ones, unless n, the amount of small spheres constitute a vast majority (n ~100%).

Therefore, the question arose how we can pinpoint the early stages of struvite formation in the absence of directly observable contributions from nano-sized species in the scattering curves that typically mark the onset of nucleation[12,13,25] (and possibly the pre-nucleation stage). To address this issue, we emphasise that our scattering data include contributions other than Porod interfaces and that one must also consider the higher-q intensity changes, resulting from the structure of the aqueous medium in association with solid (crystalline) phases. Based on Fig. 4, the evolution of the structural parameters describing different aspects of the medium are closely correlated with the progress of struvite growth. In particular, I_1 reflects the electron density weighted contribution of OZ fluctuations to scattering. As we move from a 0.1 M DAP solution at 0 s to a 0.05 M struvite "solution" at 10 s, there is a ~30% increase in I_1 (Fig. 4), indicating an increase in the "concentration" of OZ fluctuations, which we interpret as a liquid-liquid separation event[32,62,65] preceding struvite nucleation. After 10 s, the value decreases gradually over a period of ~60 s, eventually reaching a level that is ~30% lower than the initial value characteristic of 0.1 M DAP. At this point, a plateau is reached, likely corresponding to a characteristic feature of a fully equilibrated solution. Although the contribution of OZ fluctuations decreases (i.e. their "concentration" as measured by I_1), the extent of the heterogeneities expressed as ξ_{OZ} [Eq. (2)] gradually increases from the initial 0.14 nm at 0 s, to ~0.20 nm after
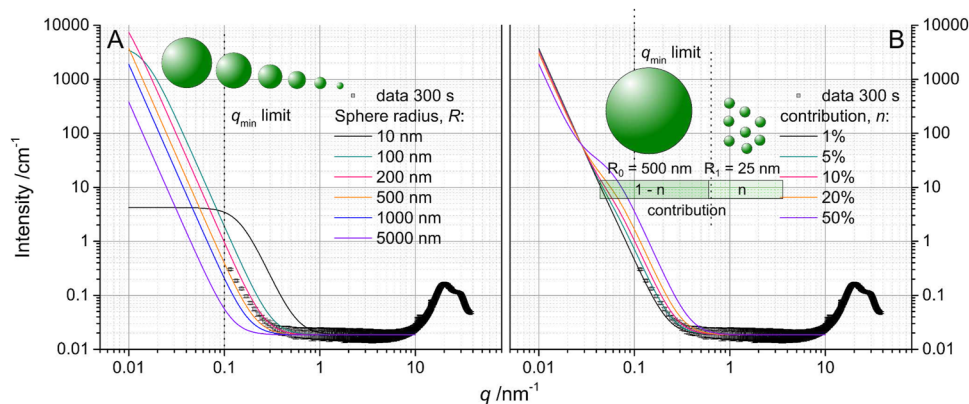
FIG. 5. (a) Simulated curves according to Eq. (3) for different sphere radii according to the labels, where $n = 0$, $\phi(\Delta\rho)^2 = 0.01$ cm^{-4}, $bkg = 0.0185$ cm^{-1}; (a) Simulated curves according to Eq. (3) for different values of the weighting factor n and $R_0 = 500$ nm, $R_1 = 25$ nm, $\phi(\Delta\rho)^2 = 0.01$ cm^{-4}, $bkg = 0.0185$ cm^{-1}.

60 s, which is a ~40% increase (Fig. 4). If we approximate ξ_{OZ} in terms of an equivalent radius of a sphere, R, the parameters follow the relationship: $R = 5/3 \cdot \sqrt{3}\,\xi_{OZ} \simeq 2.89\xi_{OZ}$ (supplementary material: Supporting Note 1). Consequently, the heterogeneities in the solvent structure initially have an equivalent diameter of 0.8 nm, and increase to ~1.1 nm concurrently with the nucleation and evolution of struvite crystals.

Lastly, the evolution of struvite causes a decrease in the I_2 parameter (Fig. 4). Following Eq. (2), I_2 approximates the intensity of the water peak at ~20 nm^{-1}. Thus, the trend shows that the maximum of this broad peak at ~20 nm^{-1} decreases at the early stages of struvite crystallisation in correlation with the growth of the diffraction peaks [Fig. 3(a), inset II]. The actual position of the peak at ~20 nm^{-1} is effectively constant, with $d = 0.311 \pm 1.0 \times 10^{-4}$ nm [insets I and II in Fig. 3(a)]. Furthermore, the scattering curves remain unchanged for $q > \sim25$ nm^{-1} [Fig. 3(a), inset II]. This all indicates that the O–O network (correlated with the peak at ~20 nm^{-1}) becomes perturbed due to the presence of evolving ionic species/precursor species, and solids as struvite evolves. We interpret this perturbation in terms of an excluded volume effect, significant enough to affect the global structure of the medium, i.e., the number density of species causing the "displacement" is large. At the same time, the second peak of water remains unaffected [Fig. 3(a), inset II], indicating that the local tetrahedral structure around the solvent is unaltered. Still, at larger distances, other species perturb the original water structure. This is in line with the PHREEQC calculations, indicating that the majority, ~54% (see Methods), of available ions remain part of the solution and do not precipitate as struvite. Classical thermodynamic models assume that unconsumed ions primarily form solvated ions. However, it is more likely that post-nucleation solutions contain also more complex species, e.g., in the form of coordination compounds, which may explain the concurrent increase in ξ_{OZ} and the decrease of I_1. This hypothesis suggests the presence of populations of nucleated entities (i.e., more complex than solvated ions) causing OZ fluctuations. As already mentioned, at 10 s, nucleation begins and leads to a short-lasting increase in both ξ_{OZ} and I_1. Again, this event can be interpreted as a liquid-liquid phase

separation where one of the separated components comprises precritical entities.[13] Larger associations of such colloidal aggregates transform/coalesce into amorphous particles/droplets observed in cryo-TEM. Another kinetic aspect to consider is the evolution of pH and the associated stability of different protonated phosphate species. Starting from basic conditions, pH ≈ 8, would lead to the stabilisation of the predominantly single-protonated HPO_4^{2-} species. Conversely, by the end of the precipitation, the drop in pH to 5.7 would shift the equilibrium to the double-protonated species $H_2PO_4^-$. The presence of different protonated phosphate ligands in aqueous solution could potentially affect the local structure of strongly hydrated amorphous metal phosphate entities, similarly as observed and proposed in calcium phosphate,[23] calcium carbonate[13] or other metal carbonates.[17] The transformation of the aggregates to a crystal occurs within seconds making it challenging to track the actual transition. Potentially, the miscibility gap characteristic of the liquid–liquid phase separation of the phosphate species in water is restricted to a very narrow concentration window, even more inhibiting the possibility to observe or capture this stage. However, looking at such early reaction stages of milliseconds to seconds, significant local concentration gradients are present, where eventually the concentration of the phosphate species dissolved in water is located in the miscibility gap, promoting an LLPS. Eventually, a post-nucleation equilibrium is reached with new populations of solids and dissolved species, as is reflected by the final scattering patterns (>60 s).

This potentially broad speciation of dissolved species leads to OZ solution heterogeneities,[66,67] which manifest themselves similarly to phase separation effects, e.g. in oil and water emulsions.[62] Figure 6 shows the scattering patterns of some aqueous solutions considered in this work. The scattering pattern of water exhibits a nearly flat plateau $I(q) \propto q^0$ at 0.0169 cm^{-1}, which is the expected value at 20 °C.[60] Strictly speaking, the water profile for ~0.3 nm^{-1} < q < ~6 nm^{-1} is not in fact a perfectly "straight line." It contains a weak structure factor feature caused by an interplay of attractive and repulsive intermolecular interactions.[54,59] The ionic aqueous solutions, on the other hand, all show a pronounced local
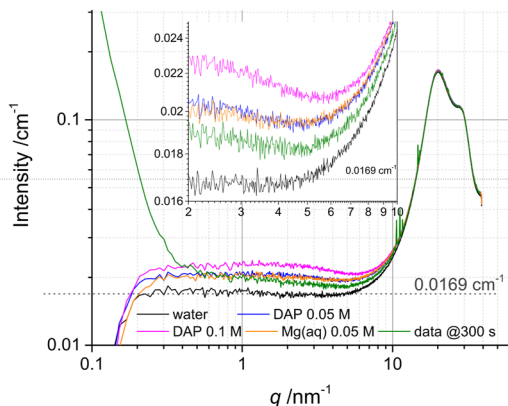
FIG. 6. Characteristic scattering patterns of several aqueous solutions and the data set, according to the labels. The inset shows in detail the scattering range $2 < q < 10 \text{ nm}^{-1}$ in where OZ fluctuations are clearly manifested.

intensity minimum, for $5 < q < 6 \text{ nm}^{-1}$ [Fig. 6, and the inset], indicating prevalent OZ fluctuations, whose magnitude [proportional to I_2 in Eq. (2)] appears to be correlated with concentrations (e.g., 0.1 vs 0.05 M DAP in Fig. 6). Our measurements on ionic aqueous solution in Fig. 6 indicate that they all contain some structural heterogeneities in the form of OZ fluctuations. When the two reactant solutions [Eq. (1), Fig. 3(a), Mg^{2+} and DAP] are mixed, the temporary miscibility gap between two liquids leads to an increase in the "concentration" of OZ heterogeneities, inducing the liquid-liquid phase separation,[13,17,45,48] resulting in the nucleation of an amorphous struvite phase and its further crystallisation.

CONCLUSIONS

In this study, we confirmed the existence of an amorphous precursor phase involved in the formation of crystalline struvite. The
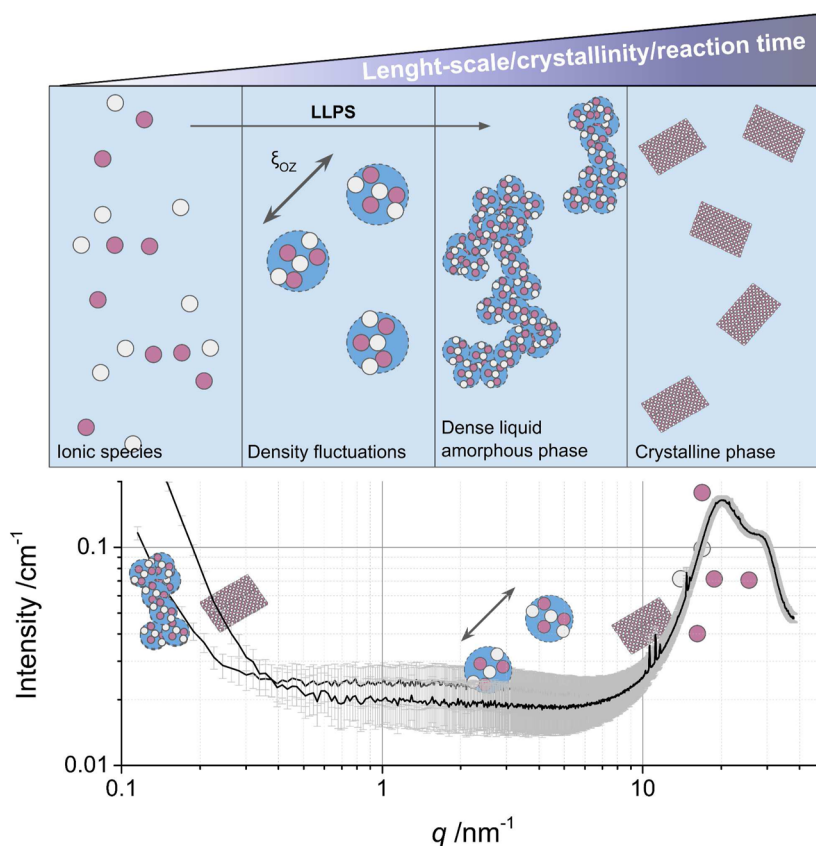
FIG. 7. The sketch summarises the evolution of entities during the crystallisation of struvite. The juxtaposition of the entities with a scattering pattern, which shows how the evolution of the solution manifests itself in scattering at different length-scales. In the schematics we do not show explicitly water molecules, but they constitute the bulk matrix of aqueous solutions and comprise solvation shells of all the other species present in solutions.

life-time of the phase is relatively short in comparison with other non-classical mineral systems.[20,49–52] Coincident with the formation of solid particles, the supramolecular structure of the aqueous solution changed during nucleation and crystallization. We interpreted the evolution of the scattering intensity and extent of the Ornstein-Zernike density fluctuations as an indicator of liquid-liquid phase separation events participating in a nucleation pathway towards crystalline struvite. These concepts are summarised in Fig. 7. Our work demonstrates for the first time that a holistic analysis of time-resolved scattering patterns is a powerful tool to follow phase separation processes, be they a liquid-liquid demixing or nucleation and growth processes.

SUPPLEMENTARY MATERIAL

The supplementary material document file contains the following items: Fig. S1. The time-resolved pH curve from the struvite precipitation reaction [Eq. (1)] combined with PHREEQC calculated equilibrated pH; Fig. S2. Cryo-TEM bright-field imaging from the reactant solution sampled after 5 s after mixing without any post-processing. Fig. S3. Sketch of the flow-through setup used for the scattering experiments; Supporting Note 1: We derive how the OZ correlation length compares with an equivalent radius of a sphere.

We also include input (MgStruvite_01_input.pqi) and output (MgStruvite_output.pqo) files from PHREEQC 3, which contain information about the predicted speciation at equilibrium following the reaction from Eq. (1). These are regular text files and are human-readable.

ACKNOWLEDGMENTS

AUTHOR DECLARATIONS

Conflict of Interest

The authors have no conflicts to disclose.

Author Contributions

Stephanos Karafiludis: Conceptualization (lead); Data curation (lead); Formal analysis (lead); Investigation (lead); Methodology (lead); Validation (lead); Visualization (lead); Writing – original draft (lead); Writing – review & editing (lead). **Ernesto Scoppola:** Data curation (supporting); Formal analysis (supporting); Investigation (supporting); Methodology (supporting); Software (equal); Validation (supporting). **Stephan E. Wolf:** Conceptualization (supporting); Formal analysis (supporting); Investigation (supporting); Methodology (supporting); Writing – original draft (supporting); Writing – review & editing (supporting). **Zdravko Kochovski:** Data curation (supporting); Formal analysis (supporting); Investigation (supporting). **David Matzdorff:** Conceptualization (supporting); Investigation (supporting). **Alexander E.**

S. Van Driessche: Conceptualization (supporting); Formal analysis (supporting); Investigation (supporting); Methodology (supporting); Validation (supporting); Writing – original draft (supporting); Writing – review & editing (supporting). **Jörn Hövelmann:** Conceptualization (supporting); Investigation (supporting); Methodology (supporting). **Franziska Emmerling:** Conceptualization (supporting); Funding acquisition (supporting); Investigation (supporting); Resources (supporting); Supervision (supporting); Writing – original draft (supporting); Writing – review & editing (supporting). **Tomasz M. Stawski:** Conceptualization (lead); Data curation (lead); Formal analysis (lead); Funding acquisition (lead); Investigation (lead); Methodology (lead); Project administration (lead); Resources (lead); Supervision (lead); Validation (lead); Visualization (lead); Writing – original draft (lead); Writing – review & editing (lead).

DATA AVAILABILITY

The data that support the findings of this study are available from the corresponding authors upon reasonable request.

REFERENCES

[1] A. Uysal, Y. D. Yilmazel, and G. N. Demirer, "The determination of fertilizer quality of the formed struvite from effluent of a sewage sludge anaerobic digester," J. Hazard. Mater. **181**(1), 248–254 (2010).

[2] G. El Diwani, Sh. El Rafie, N. N. El Ibiari, and H. I. El-Aila, "Recovery of ammonia nitrogen from industrial wastewater treatment as struvite slow releasing fertilizer," Desalination **214**(1), 200–214 (2007).

[3] S. Kratz, C. Vogel, and C. Adam, "Agronomic performance of P recycling fertilizers and methods to predict it: A review," Nutr. Cycling Agroecosyst. **115**(1), 1–39 (2019).

[4] O. Krüger, K. P. Fattah, and C. Adam, "Phosphorus recovery from the wastewater stream—Necessity and possibilities," Desalin. Water Treat. **57**(33), 15619–15627 (2016).

[5] C. Kabbe and F. Kraus, "P recovery: From evolution to revolution," Fert. Int. **479**(4), 37–41 (2017).

[6] M. Sena, M. Seib, D. R. Noguera, and A. Hicks, "Environmental impacts of phosphorus recovery through struvite precipitation in wastewater treatment," J. Cleaner Prod. **280**, 124222 (2021).

[7] K. S. Le Corre, E. Valsami-Jones, P. Hobbs, and S. A. Parsons, "Phosphorus recovery from wastewater by struvite crystallization: A review," Crit. Rev. Environ. Sci. Technol. **39**(6), 433–477 (2009).

[8] H. Huang, C. Xu, and W. Zhang, "Removal of nutrients from piggery wastewater using struvite precipitation and pyrogenation technology," Bioresour. Technol. **102**(3), 2523–2528 (2011).

[9] C. Adam, "Verfahren zur Phosphorrückgewinnung aus Abwasser und Klärschlamm," in *Verwertung von Klärschlamm*, edited by O. Holm (TK Verlag, Neuruppin, 2018), pp. 166–182.

[10] H. R. Raniro, T. d. M. Soares, C. Adam, and P. S. Pavinato, "Waste-derived fertilizers can increase phosphorus uptake by sugarcane and availability in a tropical soil#," J. Plant Nutr. Soil Sci. **185**(3), 391–402 (2022).

[11] J. Hövelmann and C. V. Putnis, "In situ nanoscale imaging of struvite formation during the dissolution of natural brucite: Implications for phosphorus recovery from wastewaters," Environ. Sci. Technol. **50**(23), 13032–13041 (2016).

[12] J. J. De Yoreo, P. U. P. A. P. A. Gilbert, N. A. J. M. J. M. Sommerdijk, R. L. Penn, S. Whitelam, D. Joester, H. Zhang, J. D. Rimer, A. Navrotsky, J. F. Banfield, A. F. Wallace, F. M. Michel, F. C. Meldrum, H. Colfen, P. M. Dove, H. Cölfen, and P. M. Dove, "Crystallization by particle attachment in synthetic, biogenic, and geologic environments," Science **349**(6247), aaa6760 (2015).

[13] D. Gebauer and S. E. Wolf, "Designing solid materials from their solute state: A shift in paradigms toward a holistic approach in functional materials chemistry," J. Am. Chem. Soc. **141**(11), 4490–4504 (2019).

[14] A. Fernandez-Martinez, H. Lopez-Martinez, and D. Wang, *New Perspect. Miner. Nucleation Growth* (Springer International Publishing, Cham, 2017), pp. 77–92.

[15] J. T. Avaro, S. L. P. Wolf, K. Hauser, and D. Gebauer, "Stable prenucleation calcium carbonate clusters define liquid–liquid phase separation," Angew. Chem., Int. Ed. **59**(15), 6155–6159 (2020).

[16] P. J. M. Smeets, K. R. Cho, R. G. E. Kempen, N. A. J. M. Sommerdijk, and J. J. De Yoreo, "Calcium carbonate nucleation driven by ion binding in a biomimetic matrix revealed by in situ electron microscopy," Nat. Mater. **14**(4), 394–399 (2015).

[17] S. E. Wolf, L. Müller, R. Barrea, C. J. Kampf, J. Leiterer, U. Panne, T. Hoffmann, F. Emmerling, and W. Tremel, "Carbonate-coordinated metal complexes precede the formation of liquid amorphous mineral emulsions of divalent metal carbonates," Nanoscale **3**(3), 1158–1165 (2011).

[18] H. Birkedal, *New Perspect. Miner. Nucleation Growth* (Springer International Publishing, Cham, 2017), pp. 199–210.

[19] J. M. Delgado-López and A. Guagliardi, *New Perspect. Miner. Nucleation Growth* (Springer International Publishing, Cham, 2017), pp. 211–225.

[20] S. Karafiludis, A. G. Buzanich, Z. Kochovski, I. Feldmann, F. Emmerling, and T. M. Stawski, "Ni- and Co-struvites: Revealing crystallization mechanisms and crystal engineering toward applicational use of transition metal phosphates," Cryst. Growth Des. **22**(7), 4305–4315 (2022).

[21] S. Jiang, W. Jin, Y.-N. Wang, H. Pan, Z. Sun, and R. Tang, "Effect of the aggregation state of amorphous calcium phosphate on hydroxyapatite nucleation kinetics," RSC Adv. **7**(41), 25497–25503 (2017).

[22] F. Nudelman, K. Pieterse, A. George, P. H. H. Bomans, H. Friedrich, L. J. Brylka, P. A. J. Hilbers, G. de With, and N. A. J. M. Sommerdijk, "The role of collagen in bone apatite formation in the presence of hydroxyapatite nucleation inhibitors," Nat. Mater. **9**(12), 1004–1009 (2010).

[23] L. Wang, S. Li, E. Ruiz-Agudo, C. V. Putnis, and A. Putnis, "Posner's cluster revisited: Direct imaging of nucleation and growth of nanoscale calcium phosphate clusters at the calcite-water interface," CrystEngComm **14**(19), 6252–6256 (2012).

[24] T. M. Stawski, A. E. S. A. E. S. van Driessche, M. Ossorio, J. Diego Rodriguez-Blanco, R. Besselink, and L. G. L. G. Benning, "Formation of calcium sulfate through the aggregation of sub-3 nanometre primary species," Nat. Commun. **7**, 11177 (2016).

[25] A. E. S. Van Driessche, T. M. Stawski, L. G. Benning, and M. Kellermeier, *New Perspect. Miner. Nucleation Growth* (Springer International Publishing, Cham, 2017), pp. 227–256.

[26] F. Jones, "Infrared investigation of barite and gypsum crystallization: Evidence for an amorphous to crystalline transition," CrystEngComm **14**(24), 8374–8381 (2012).

[27] Y.-W. Wang, Y.-Y. Kim, H. K. Christenson, and F. C. Meldrum, "A new precipitation pathway for calcium sulfate dihydrate (gypsum) via amorphous and hemihydrate intermediates," Chem. Commun. **48**(4), 504–506 (2012).

[28] J. Scheck, B. Wu, M. Drechsler, R. Rosenberg, A. E. S. A. E. S. Van Driessche, T. M. Stawski, and D. Gebauer, "The molecular mechanism of iron(III) oxide nucleation," J. Phys. Chem. Lett. **7**(16), 3123–3130 (2016).

[29] J. S. Weatherill, K. Morris, P. Bots, T. M. Stawski, A. Janssen, L. Abrahamsen, R. Blackham, and S. Shaw, "Ferrihydrite formation: The role of Fe13 Keggin clusters," Environ. Sci. Technol. **50**(17), 9333–9342 (2016).

[30] J. Baumgartner, A. Dey, P. H. H. Bomans, C. Le Coadou, P. Fratzl, N. A. J. M. Sommerdijk, and D. Faivre, "Nucleation and growth of magnetite from solution," Nat. Mater. **12**(4), 310–314 (2013).

[31] K. Ashley, D. Mavinic, and F. Koch, *International Conference on Nutrient Recovery from Wastewater Streams Vancouver, 2009* (IWA Publishing, 2009).

[32] S. Xu, H. Zhang, B. Qiao, and Y. Wang, "Review of liquid–liquid phase separation in crystallization: From fundamentals to application," Cryst. Growth Des. **21**(12), 7306–7325 (2021).

[33] D. L. Parkhurst and C. A. J. Appelo, *Description of Input and Examples for PHREEQC Version 3: A Computer Program for Speciation, Batch-Reaction, One-Dimensional Transport, and Inverse Geochemical Calculations* (US Geological Survey, 2013).

[34] J. W. Ball and D. K. Nordstrom, *User's Manual for WATEQ4F, with Revised Thermodynamic Data Base and Text Cases for Calculating Speciation of Major, Trace, and Redox Elements in Natural Waters* (U.S. Geological Survey, 1991).

[35] C. M. Mehta and D. J. Batstone, "Nutrient solubilization and its availability following anaerobic digestion," Water Sci. Technol. **67**(4), 756–763 (2013).

[36] M. I. H. Bhuiyan, D. S. Mavinic, and R. D. Beckie, "A solubility and thermodynamic study of struvite," Environ. Technol. **28**(9), 1015–1026 (2007).

[37] I. Zizak, "The mySpot beamline at BESSY II," J. Large-Scale Res. Facil. **2**, A102 (2016).

[38] G. Ashiotis, A. Deschildre, Z. Nawaz, J. P. Wright, D. Karkoulis, F. E. Picca, and J. Kieffer, "The fast azimuthal integration Python library:pyFAI," J. Appl. Crystallogr. **48**(2), 510–519 (2015).

[39] P. H. Eilers and H. F. Boelens, "Baseline correction with asymmetric least squares smoothing," Leiden Univ. Med. Cent. Rep. **1**(1), 5 (2005).

[40] J. Peng, S. Peng, A. Jiang, J. Wei, C. Li, and J. Tan, "Asymmetric least squares for multiple spectra baseline correction," Anal. Chim. Acta **683**(1), 63–68 (2010).

[41] C. T. Rueden, J. Schindelin, M. C. Hiner, B. E. DeZonia, A. E. Walter, E. T. Arena, and K. W. Eliceiri, "ImageJ2: ImageJ for the next generation of scientific image data," BMC Bioinf. **18**(1), 529 (2017).

[42] G. Ferraris, H. Fuess, and W. Joswig, "Neutron diffraction study of MgNH$_4$PO$_4$ · 6H$_2$O (struvite) and survey of water molecules donating short hydrogen bonds," Acta Crystallogr., Sect. B: Struct. Sci. **42**(3), 253–258 (1986).

[43] Y. Kimura, H. Katsuno, and T. Yamazaki, "Possible embryos and precursors of crystalline nuclei of calcium carbonate observed by liquid-cell transmission electron microscopy," Faraday Discuss. **235**, 81–94 (2022).

[44] V. Ramnarain, T. Georges, N. Ortiz Peña, D. Ihiawakrim, M. Longuinho, H. Bulou, C. Gervais, C. Sanchez, T. Azaïs, and O. Ersen, "Monitoring of CaCO$_3$ nanoscale structuration through real-time liquid phase transmission electron microscopy and hyperpolarized NMR," J. Am. Chem. Soc. **144**(33), 15236–15251 (2022).

[45] S. E. Wolf, J. Leiterer, M. Kappl, F. Emmerling, and W. Tremel, "Early homogenous amorphous precursor stages of calcium carbonate and subsequent crystal growth in levitated droplets," J. Am. Chem. Soc. **130**(37), 12342–12347 (2008).

[46] H. Cölfen and L. Qi, "A systematic examination of the morphogenesis of calcium carbonate in the presence of a double-hydrophilic block copolymer," Chem.-Eur. J. **7**(1), 106–116 (2001).

[47] C. Rodriguez-Navarro, K. Kudłacz, Ö. Cizer, and E. Ruiz-Agudo, "Formation of amorphous calcium carbonate and its transformation into mesostructured calcite," CrystEngComm **17**(1), 58–72 (2015).

[48] A. F. Wallace, L. O. Hedges, A. Fernandez-Martinez, P. Raiteri, J. D. Gale, G. A. Waychunas, S. Whitelam, J. F. Banfield, and J. J. De Yoreo, "Microscopic evidence for liquid-liquid separation in supersaturated CaCO$_3$ solutions," Science **341**(6148), 885–889 (2013).

[49] E. Ruiz-Agudo, A. Burgos-Cara, C. Ruiz-Agudo, A. Ibañez-Velasco, H. Cölfen, and C. Rodriguez-Navarro, "A non-classical view on calcium oxalate precipitation and the role of citrate," Nat. Commun. **8**(1), 768 (2017).

[50] G. Montes-Hernandez, F. Renard, A.-L. Auzende, and N. Findling, "Amorphous calcium–magnesium carbonate (ACMC) accelerates dolomitization at room temperature under abiotic conditions," Cryst. Growth Des. **20**(3), 1434–1441 (2020).

[51] T. M. Stawski, A. E. S. Van Driessche, R. Besselink, E. H. Byrne, P. Raiteri, J. D. Gale, and L. G. Benning, "The structure of CaSO$_4$ nanorods: The precursor of gypsum," J. Phys. Chem. C **123**(37), 23151–23158 (2019).

[52] Z. Zou, J. Xie, E. Macías-Sánchez, and Z. Fu, "Nonclassical crystallization of amorphous calcium carbonate in the presence of phosphate ions," Cryst. Growth Des. **21**(1), 414–423 (2021).

[53] G. Hura, J. M. Sorenson, R. M. Glaeser, and T. Head-Gordon, "A high-quality x-ray scattering experiment on liquid water at ambient conditions," J. Chem. Phys. **113**(20), 9140–9148 (2000).

[54] G. N. I. Clark, G. L. Hura, J. Teixeira, A. K. Soper, and T. Head-Gordon, "Small-angle scattering and the structure of ambient liquid water," Proc. Natl. Acad. Sci. U. S. A. **107**(32), 14003–14007 (2010).

[55] G. Hura, D. Russo, R. M. Glaeser, T. Head-Gordon, M. Krack, and M. Parrinello, "Water structure as a function of temperature from X-ray scattering experiments and *ab initio* molecular dynamics," Phys. Chem. Chem. Phys. **5**(10), 1981–1991 (2003).

[56] M. B. de Kock, S. Azim, G. H. Kassier, and R. J. D. Miller, "Determining the radial distribution function of water using electron scattering: A key to solution phase chemistry," J. Chem. Phys. **153**(19), 194504 (2020).

[57] T. Head-Gordon and M. E. Johnson, "Tetrahedral structure or chains for liquid water," Proc. Natl. Acad. Sci. **103**(21), 7973–7977 (2006).

[58] S. R. Elliott, "Interpretation of the principal diffraction peak of liquid and amorphous water," J. Chem. Phys. **103**(7), 2758–2761 (1995).

[59] C. Huang, K. T. Wikfeldt, T. Tokushima, D. Nordlund, Y. Harada, U. Bergmann, M. Niebuhr, T. M. Weiss, Y. Horikawa, M. Leetmaa, M. P. Ljungberg, O. Takahashi, A. Lenz, L. Ojamäe, A. P. Lyubartsev, S. Shin, L. G. M. Pettersson, and A. Nilsson, "The inhomogeneous structure of water at ambient conditions," Proc. Natl. Acad. Sci. **106**(36), 15214–15218 (2009).

[60] D. Orthaber, A. Bergmann, and O. Glatter, "SAXS experiments on absolute scale with Kratky systems using water as a secondary standard," J. Appl. Crystallogr. **33**(2), 218–225 (2000).

[61] L. S. Ornstein and F. Zernike, "Accidental deviations of density and opalescence at the critical point of a single substance," K. Ned. Akad. Van Wet. Proceedings **17**, 793–806 (1914).

[62] S. Prevost, T. Lopian, M. Pleines, O. Diat, and T. Zemb, "Small-angle scattering and morphologies of ultra-flexible microemulsions," J. Appl. Crystallogr. **49**(6), 2063–2072 (2016).

[63] R. Besselink, T. M. Stawski, A. E. S. Van Driessche, and L. G. Benning, "Not just fractal surfaces, but surface fractal aggregates: Derivation of the expression for the structure factor and its applications," J. Chem. Phys. **145**(21), 211908 (2016).

[64] G. Porod, "Die Abhängigkeit der Röntgen-kleinwinkelstreuung von Form und Grösse der Kolloiden Teilchen in verdünnten Systemen, IV," Acta Phys. Austriaca **2**, 255–292 (1948).

[65] P. R. t. Wolde and D. Frenkel, "Enhancement of protein crystal nucleation by critical density fluctuations," Science **277**(5334), 1975–1978 (1997).

[66] A. Dixit, S. B. Majumder, A. Savvinov, R. S. Katiyar, R. Guo, and A. S. Bhalla, "Investigations on the sol-gel-derived barium zirconium titanate thin films," Mater. Lett. **56**(6), 933–940 (2002).

[67] A. Perera and B. Kežić, "Fluctuations and micro-heterogeneity in mixtures of complex liquids," Faraday Discuss. **167**, 145–158 (2013).

25 January 2024 09:08:28